



Supercritical combustion of gas-centered liquid-swirl coaxial injectors for staged-combustion engines

Xingjian Wang, Liwei Zhang, Yixing Li, Shiang-Ting Yeh, Vigor Yang*

Daniel Guggenheim School of Aerospace Engineering, Georgia Institute of Technology, Atlanta, Georgia 30332, USA



ARTICLE INFO

Article history:

Received 16 February 2018

Revised 19 April 2018

Accepted 19 July 2018

Keywords:

Supercritical combustion
Gas-liquid swirl injector
Rocket injector
Staged-combustion engine

ABSTRACT

The combustion characteristics of gas-centered, liquid-swirl coaxial injectors typically used in oxidizer-rich staged combustion cycle engines are numerically investigated at supercritical conditions. Turbulence closure is achieved using large-eddy-simulation techniques, and turbulence/chemistry interaction is modeled by a steady laminar flamelet approach. Gaseous oxygen (GOX) at 687.7 K is injected into the center post while kerosene at 492.2 K is delivered tangentially into the outer coaxial annulus. The operating pressure is 25.3 MPa. Detailed flow structures and flame dynamics are explored. The entire flowfield can be divided into four regimes: propellant injection, flame initialization, flame development, and intensive combustion. The diffusion-dominated flame is anchored in the wake of the GOX post and further enhanced in the downstream taper region. The surface of the coaxial annulus and taper is covered by fuel-rich mixtures and thus protected from thermal flux in the flame zone. Effects of the recess length (from the end of GOX post to the entrance of taper region) on the flow and flame evolution are investigated in depth. The efficiency of propellant mixing and subsequent combustion is found to increase with increasing recess length. The kerosene film is nearly depleted before the exit of the recess region for cases with long recess length, and the flame spreads upwards in the taper region for cases with reduced recess length due to insufficient mixing between GOX and kerosene. In a fully recessed injector without fuel shielding, the injected kerosene behaves like a liquid jet in a crossflow. Two recirculating zones containing fuel-rich mixtures are formed between the injection slit and the headend. A broad flame region is established at the exit of the recess region. In a non-recessed injector, the occurrence of combustion is delayed to the taper region. The flame resides along the taper surface and the injector faceplate, with most of GOX convecting downstream unburned. Results obtained from the present study can also be used to characterize combustion responses to local flow oscillations.

© 2018 The Combustion Institute. Published by Elsevier Inc. All rights reserved.

1. Introduction

This paper deals with the combustion characteristics of gas-centered liquid-swirl coaxial (GCLSC) injectors, as shown in Fig. 1. High-temperature gaseous oxygen (GOX) is injected into the center post, while liquid kerosene is delivered tangentially into the coaxial annulus. The swirl-induced centrifugal force causes the cold liquid to flow through the annulus and consequently provide necessary cooling and protection of the injector surface from hot combustor products. The gaseous core also acts as an acoustic resonator to transmit acoustic energy from the combustion chamber to the GOX manifold. This type of injector has been broadly employed in the main combustion chambers of several high-performance, high-thrust liquid rocket engines, such as NK-

33, RD-120, and RD-170/180 engines [1]. It remains a primary candidate for future applications worldwide, especially for oxidizer-rich staged combustion (ORSC) cycle engines using liquid oxygen (LOX) and hydrocarbon fuels as propellants.

Although GCLSC injectors have been successfully implemented in various propulsion engines, understanding of the key physics of propellant injection, mixing, and combustion remains limited. It is well-established that injectors exert a strong influence on the dynamics and stability of a combustion system, due to the feedback coupling between the combustion chamber and other engine components through the injection process [2,3]. The current injector design practice, however, is primarily an empirical, resource-consuming endeavor, and depends strongly on the history of the engine program in question [1]. Furthermore, any given class or family of injectors is usually designed for a specific application associated with propellant type and operational requirements. A comprehensive knowledge of flow and flame dynamics is thus required to support innovation in injector design and optimization.

* Corresponding author.

E-mail addresses: xwang343@gatech.edu (X. Wang), vigor.yang@aerospace.gatech.edu (V. Yang).

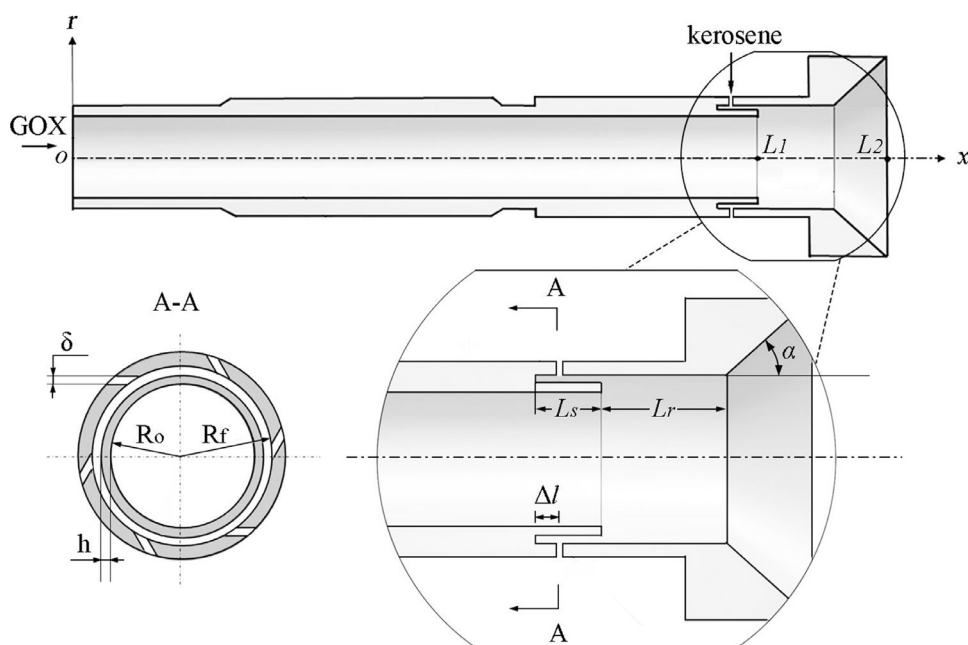


Fig. 1. Schematic of GOX/kerosene GCLSC injector.

Experimental studies on GCLSC injectors have historically been conducted mainly at low or moderate pressures. Miller et al. [4] investigated the stability behavior of a water-oxygen and kerosene system as a function of chamber length over a pressure range of 2.14–2.38 MPa. Sisco et al. [5] extended the work by varying oxidizer tube length and inlet type under similar operating conditions. The corresponding influences on acoustic properties in the oxidizer tube and combustion chamber were examined. Yu et al. [6] redesigned the test rig of Sisco et al. [5] as a continuously variable resonance combustor, which allowed observation of both stable and unstable behaviors at a pressure of 1.3 MPa in a single firing test with gaseous methane as fuel. The experiments provided a useful database for validating numerical simulations [7,8], which in turn extracted more detailed flow structures and dynamics in the combustor. The operating pressure, however, was significantly below the nominal chamber pressures of liquid rocket engines, such as, for example, 25.3 MPa for the RD-170 main chamber [9]. Recently, Ballance et al. [10] performed high-speed optical diagnostics of a GCLSC injector in a high-pressure combustor with GOX and liquid kerosene RP-2 as propellants. Data were obtained with pressures from 2.0 to 16.5 MPa. The mixture ratio covers a range of 2.9–20.0. Side-on chemiluminescence and infrared images were obtained. In addition, a novel borescope was employed to image the flame from upstream of the GOX post, enabling visualization of the flame in its stabilization location. Their work provides the first, and most comprehensive to date, optical measurement of the flame structures and dynamics at a scale sufficient to identify the flame anchoring and associated flow evolution.

Ahn and colleagues [11,12] studied the combustion characteristics of LOX/kerosene bi-swirl injectors at pressures up to 8 MPa. The recess of the inner swirler from the injector exit was shown to play a major role in determining combustion performance at both subcritical and supercritical pressures. Wang and colleagues [13,14] numerically investigated the flow and flame development of LOX/kerosene bi-swirl injectors at supercritical pressures. The flame was stabilized by two-counter rotating flows in the wake of the LOX post. The width of the kerosene annulus was found to have significant influence on flame stabilization and subsequent spreading. Soller et al. [15] performed a number of hot-fire tests of an oxygen/kerosene single-element rocket injector in the pressure

range of 4.0–8.5 MPa and mixture ratios of 2.4–3.5. Combustion efficiency and stability characteristics were examined.

Although much information has been established for bi-swirl injectors, very limited experimental and numerical studies are available in the literature on GCLSC injectors at the supercritical conditions typical of practical rocket engine operation [10]. The present work attempts to explore numerically the combustion characteristics of a GCLSC injector for a GOX/kerosene system under conditions mimicking the operation of the main combustion chamber of an ORSC engine RD-170/180 [1,9]. A unified theoretical/numerical framework based on large-eddy-simulation techniques is implemented, along with a steady laminar flamelet approach. The flow dynamics and mixing of this injector are systematically investigated in companion studies [16,17]. The present work examines the underlying physiochemical processes associated with flame stabilization and development, with special attention to the near-field evolution downstream of the GOX post. The effects of recess on flame characteristics are studied in depth.

2. Theoretical and numerical framework

The theoretical formulation of the present study is described in Oefelein and Yang [18] and Yang [19]; these studies deal with supercritical fluid flows and combustion over the entire range of fluid thermodynamic states of concern. Turbulence closure is achieved using the large eddy simulation (LES) technique. A compressible-version of Smagorinsky model is employed to characterize the effects of subgrid-scale motion. Thermodynamic properties, including density, enthalpy, and specific heat at constant pressure, are evaluated according to fundamental thermodynamics theories and a modified Soave-Redlich-Kwong equation of state. Transport properties, including thermal conductivity and dynamic viscosity, are estimated using extended corresponding-state principles. Mass diffusivity is obtained by the Takahashi method calibrated for high-pressure conditions. The evaluation of thermodynamic and transport properties has been validated and implemented in previous studies [19].

Modeling turbulence/chemistry interactions remains a critical issue. A precise classification of turbulent diffusion flame regimes is still an open research field, due to the lack of well-defined

length, time, and velocity scales [20]. The local flame scales depend on local flow conditions. Further, the chemical kinetics of kerosene combustion involve hundreds of species and thousands of elementary reaction steps, rendering direct simulation of detailed chemistry computationally prohibitive. A steady laminar flamelet model is applied in the present study. The underlying assumption is that the local Damkohler number ($Da^fl = \tau_f / \tau_c$), where τ_f and τ_c are the flow characteristic and chemical time, respectively, is sufficiently large and the chemistry is sufficiently fast to follow the flow changes. Unsteady effects and flame extinction take place when Da^fl is low. As will be shown later, the local strain rate in the flowfield of concern in the present work is much smaller than the extinction strain rate ($\sim 10^7 \text{ s}^{-1}$ at 25 MPa) for oxygen/kerosene counterflow diffusion flames [21]. This implies that Da^fl is sufficiently large, and justifies the use of the flamelet approach. A detailed description of implementation of the flamelet approach can be found in our previous work [14,22] and is not included here.

A three-component surrogate (n-decane/n-propylbenzene/n-propylcyclohexane with 74/15/11% by volume) for kerosene [23] has shown good agreement with jet-stirred reactor data and is thus employed here. A skeletal mechanism with 106 species and 382 reactions developed by Wang et al. [24] is implemented because of its computational efficiency and high accuracy in predicting global combustion characteristics for a pressure range of 0.1–2.0 MPa and an equivalence-ratio range of 0.5–1.5. It is noted that the operating pressure in the present work is around 25 MPa. Further validation may be required to determine whether this skeletal mechanism is suitable at such elevated pressure. In spite of this, earlier studies [21,25] revealed general similarities of flame properties in terms of flame temperature, flame thickness, species concentrations, reaction rates, and heat release rate for counterflow diffusion flames over a wide range of pressures. The flame solutions at high pressure can be evaluated according to their counterpart at low pressure using a priori mapping along the stable-burning branch of the S-curve in the range of strain rates considered in the present work. The species mass fractions are extracted from the flame solutions and filtered by convolution with the joint PDF of the mixture fraction and scalar dissipation rate, and stored in the flamelet library. Beta- and Dirac-delta functions are selected for the filter PDFs of the mixture fraction and scalar dissipation rate, respectively. Given the filtered mixture fraction, variance of the mixture fraction, and scalar dissipation rate from the turbulent field, the species mass fractions are retrieved from the flamelet library. Figure 2 shows the interaction between the flow solver and flamelet library.

The numerical framework was established by implementing a preconditioning scheme and a unified treatment of general-fluid thermodynamics [26]. It employs a density-based, finite-volume methodology, along with a dual-time-step integration technique [27,28]. Temporal discretization is achieved using a second-order backward difference, and the inner-loop pseudo-time term is integrated with a four-step Runge-Kutta scheme. Spatial discretization is obtained using a fourth-order central difference scheme in generalized coordinates. Fourth-order matrix dissipation is taken to ensure numerical stability and minimum contamination of the solution. Finally, a multi-block domain decomposition technique associated with the message passing interface technique of parallel computing is applied to optimize computation speed.

3. Injector configuration and boundary conditions

Figure 1 shows the GCLSC injector of concern, which mimics the injector for the main combustion chamber of the LOX/kerosene staged combustion rocket engine, RD-170/180 [1,9]. The injector consists of four regions: the center cylindrical tube, coaxial annu-

Table 1
Geometric parameters of baseline injector (Case 3).

δ (mm)	$h1$ (mm)	Ro (mm)	h (mm)	Rf (mm)
0.60	5.75	5.62	0.745	7.03
$L1$ (mm)	$L2$ (mm)	Ls (mm)	Δl (mm)	α
93	113.1	5.5	2.0	42°

Table 2
Recess and shielding lengths.

Cases	1	2	3	4	5	6
L_r (mm)	16	13	10.5	7	3.5	0
L_s (mm)	0	3	5.5	9	12.5	16

Table 3
Injector operating conditions.

\dot{m}_o (kg/s)	\dot{m}_f (kg/s)	$T_{in,o}$ (K)	$T_{in,f}$ (K)	p_a (MPa)
1.33	0.477	687.7	492.2	25.3

lus, recess, and taper regions. GOX is injected axially into the center tube (known as GOX post), and liquid kerosene is tangentially introduced into the coaxial annulus through a total of 12 circular fuel holes. These holes are simplified to a circular slit located at $\Delta l = 2.0$ mm downstream of the annulus headend. Table 1 lists the geometric parameters of the injector. The GOX post thickness (h) is 0.745 mm. The recess region, from the end of the GOX post to the entrance of the taper region, has been shown to have significant effects on the flame stabilization characteristics [1]. The mixing of GOX and kerosene begins in the recess region and intensifies in the taper region and downstream of the injector [16]. In the present work, six different recess lengths (L_r) are considered in a range of 0–16 mm. The length of the annulus outer surface is fixed at 16 mm, and the length of the annulus inner surface (kerosene fuel shielding, L_s) varies according to the length of recess, L_r . Table 2 lists the lengths of recess and shielding for the six different cases. The recess length decreases with increasing case number. Case 3, with a recess length of 5.5 mm, is considered as the baseline, while Case 1 is fully recessed and Case 6 has no recess.

To isolate the effect of recess length, the operating conditions remain identical for all cases, as listed in Table 3. \dot{m}_o and \dot{m}_f represent the mass flow rate of GOX and kerosene fuel, respectively; $T_{in,o}$ and $T_{in,f}$ the corresponding injection temperature, respectively. The operating pressure is denoted as p_a . The nominal momentum flux ratio between the oxidizer and fuel streams is estimated as $\rho_o U_o^2 / \rho_f U_f^2$. The densities of oxidizer and fuel at the injection point are 131 and 640 kg/m³, respectively. The reference axial velocity of the GOX stream is calculated as 102 m/s. The reference velocity of kerosene needs to be evaluated carefully. For Case 1, without shielding, the kerosene radially penetrates into the axial GOX stream, behaving like liquid injection in a crossflow. U_f is taken as the radial velocity component at the inlet, 24.5 m/s. For cases with shielding, U_f is most appropriately represented by the axial velocity in the coaxial annulus, 26.6 m/s. The momentum flux ratio is thus obtained as 3.5 for Case 1 and 3.0 for Cases 2–6.

The computational domain consists of the injector interior ($18R_o$ in the axial direction) and a downstream region ($25R_o$ and $7R_o$ in the axial and radial directions, respectively). As mentioned earlier, axisymmetric calculations are carried out because of the large computational cost of simulating the flame evolution in the entire three-dimensional domain. A cylindrical sector is considered, with periodic boundary conditions specified in the azimuthal direction. This leads to the exclusion of the vortex-stretching mechanism responsible for turbulent energy transfer from large to small eddies. In spite of this simplification, previ-

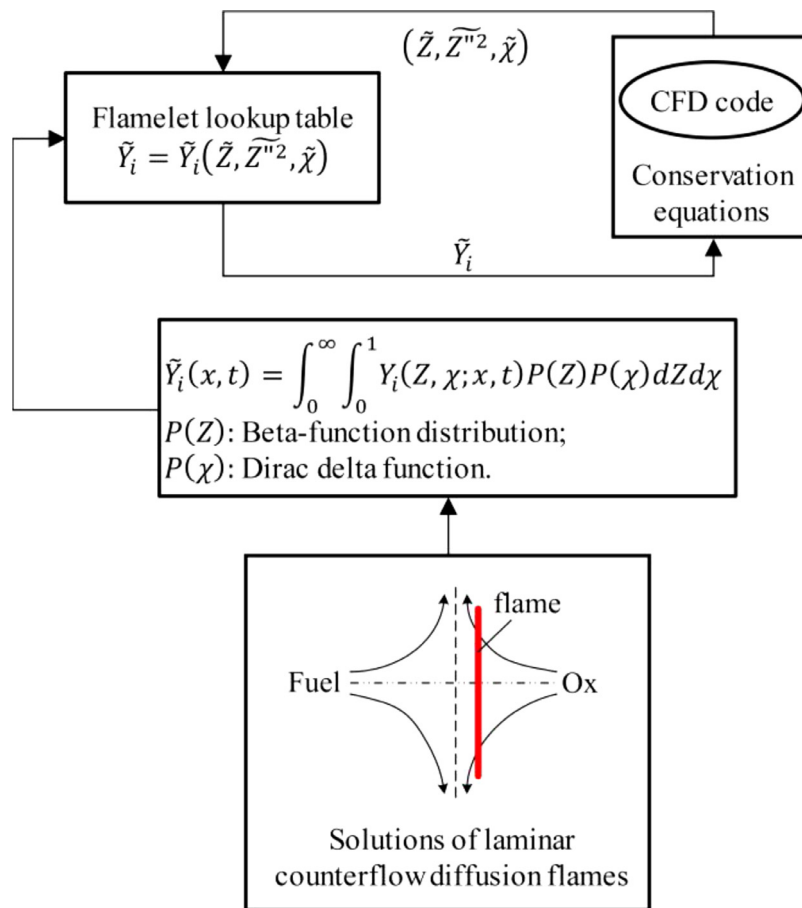


Fig. 2. Interaction between flow solver and flamelet library.

ous studies have shown that the present method is able to capture many of the salient features of supercritical flows [14,29,30]. (Note that a three-dimensional combustion study should be conducted in the future to capture transverse flow instabilities.) An acoustically non-reflecting boundary condition [31] is implemented at the entrance of the GOX post. The downstream boundary in both the axial and radial directions is treated with the method of characteristics [32] combined with the use of buffer zones [33]. No-slip and adiabatic boundary conditions are enforced at the injector surface. A reference pressure is applied to preserve the average pressure in the computational domain.

4. Results and discussion

In order to ensure appropriate numerical resolution, the grid system employed here was validated through a grid independence study similar to the one described in [16] for the same geometry and flow conditions. Three different levels of resolution were tested, with the grid size reduced by half at each level. The total number of grid points varied from 58,000 for the coarsest level to 928,000 for the finest level. The mean flow profile distributions showed good agreement for all three levels. Although the finest level can capture the details of small turbulent eddies, the intermediate level, with 232,000 grid points, was selected based on the tradeoff between computational efficiency and numerical accuracy. The smallest grid size is 5 μm , as compared to the Taylor scale of 10 μm within the injector.

Figure 3 shows a global view of instantaneous temperature distributions for Cases 1, 3, and 6. The geometry-dependent flame dynamics are clearly observed. The entire flowfield can be divided

into four regimes: propellant injection, flame initialization, flame development, and intensive combustion, as shown schematically in Fig. 4. The injection regime consists primarily of the center tube and coaxial annulus, where GOX and kerosene are injected separately. The flame is initialized and anchored in the wake of the GOX post and develops further in the recess region. Intensive combustion then takes place and becomes well-distributed in the downstream region for the cases with recess region. For Case 6 without recess, the interaction of GOX and kerosene is delayed to the taper region. Combustion resides primarily in the upper end of the downstream region close to the injector faceplate, because of the insufficient entrainment of kerosene into the GOX stream.

To justify the combustion model employed in the present work, Fig. 5 shows the instantaneous distributions of the flame index and magnitude of local flow strain rate for Cases 1 and 3. The flame index (defined as $G = \nabla Y_f \nabla Y_o$, with Y_f and Y_o being the mass fractions of fuel and oxidizer, respectively) is generally used to distinguish non-premixed from premixed flames [34]. In the present study, it is found that the flame index is primarily negative for both cases, implying that the overall burning process is in the non-premixed mode. The flame can thus be viewed as an ensemble of diffusion flamelets stretched and contorted by the turbulent flow. The magnitude of the local flow strain rate is around 10^5 – 10^6 s^{-1} as shown in Fig. 5, consistently lower than the extinction strain rate ($\sim 10^7 \text{ s}^{-1}$) [21]. Similar results are obtained for other cases. This indicates that local flame extinction is unlikely to occur, thereby verifying the use of the steady laminar flamelet model. In the following sections, the details of flow evolution and flame dynamics are discussed in the four regimes mentioned in Fig. 4.

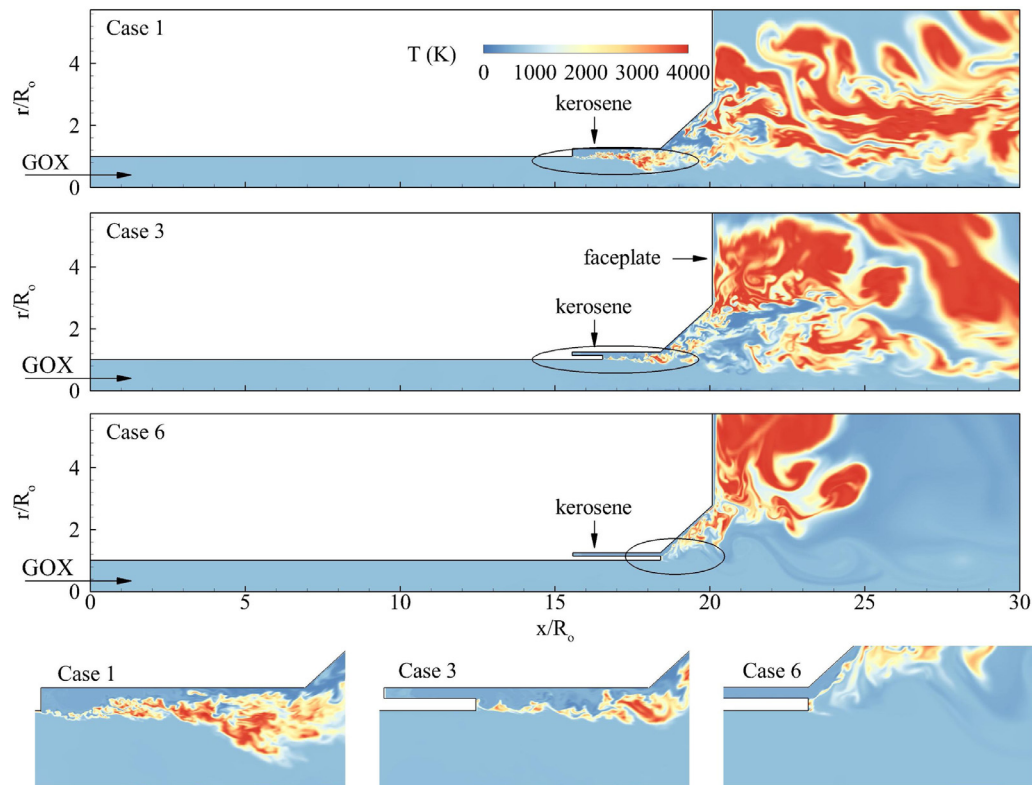


Fig. 3. Global and zoom-in views of instantaneous temperature field for Cases 1, 3, and 6.

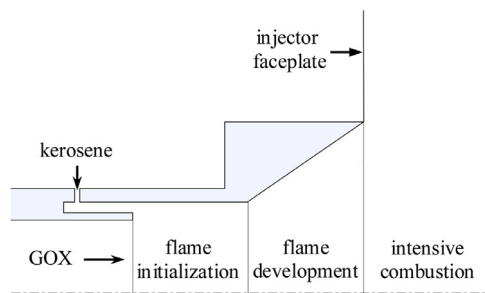


Fig. 4. Schematic of flow regimes.

4.1. Propellant injection region

Figure 6 shows the radial profiles of time-averaged axial velocity immediately downstream (Case 1) or upstream (Cases 2–6) of the GOX post tip. The vertical dashed line represents zero velocity, and the horizontal dashed line denotes the center of the coaxial annulus. The region of $1.0 < r/R_0 < 1.13$ is a continuous flow zone in Case 1, but is displaced by the fuel shielding in Cases 2–6. As the recess length decreases (the shielding length increases accordingly), the axial velocity decreases slightly within the GOX post ($r/R_0 \leq 1.0$). This is attributed partly to the pressure change in the flame zone and partly to the viscous loss along the GOX post surface with different geometries. The pressure downstream of the injection region decreases due to combustion. It results in a favorable pressure gradient between the GOX entrance and the post tip, and an increased axial velocity compared to the initial value (102 m/s). Such increment decreases with increasing fuel shielding length from Cases 1 to 6, because of the corresponding increase in viscous loss and decrease in combustion intensity. Different flow profiles are observed in the coaxial fuel annulus ($1.13 \leq r/R_0 \leq 1.25$).

Because of the lack of shielding in Case 1, kerosene is radially injected into the GOX stream, which has a stronger axial momentum. The kerosene stream must adjust its direction and merges into the GOX flow. The negative profile in the region of $1.13 \leq r/R_0 \leq 1.25$ in Fig. 6 is caused by flow reversal in the corner region.

In Cases 2 and 3 ($L_r \geq 10.5$ mm, $L_s \leq 5.5$ mm), the distribution of axial velocity in the fuel annulus resembles that of a channel flow with significant angular momentum. The shielding is too short to allow for the full development of the kerosene stream in the annulus. As the shielding length increases (Cases 4 and 5), the residence time for kerosene in the annulus increases, rendering a fully developed flow, as manifested by the axisymmetric velocity profiles in Fig. 6. In spite of the longest residence time in the fuel annulus in Case 6, the profile of the axial velocity ($L_r = 0$) is asymmetric, with the peak value located above the centerline. The phenomenon is caused by two contributing factors: (1) the kerosene stream spreads upwards due to the sudden expansion at the entrance of the taper region and the swirl-induced centrifugal force; and (2) the expansion of hot products in the wake of the GOX post drives kerosene to flow along the taper surface.

Figure 7 shows the time-averaged bulk axial momentum immediately upstream of the end of the GOX post as a function of recess length. It is obtained by integrating axial momentum flux in the radial direction. The axial momentum in the fuel annulus is not plotted for Case 1, because the fuel stream penetrates radially into the GOX flow without shielding. The axial momentum increases gradually with decreasing fuel shielding (increasing recess length) in the center tube, due to reduced viscous loss along the post surface and enhanced combustion in the downstream region. The axial momentum in the fuel annulus follows a similar trend until the recess length approaches zero, and increases slightly. This distinction is attributed to the dynamic process near the taper region when there is no recess (Case 6). The sudden expansion of the swirling kerosene stream at the entrance of the taper region

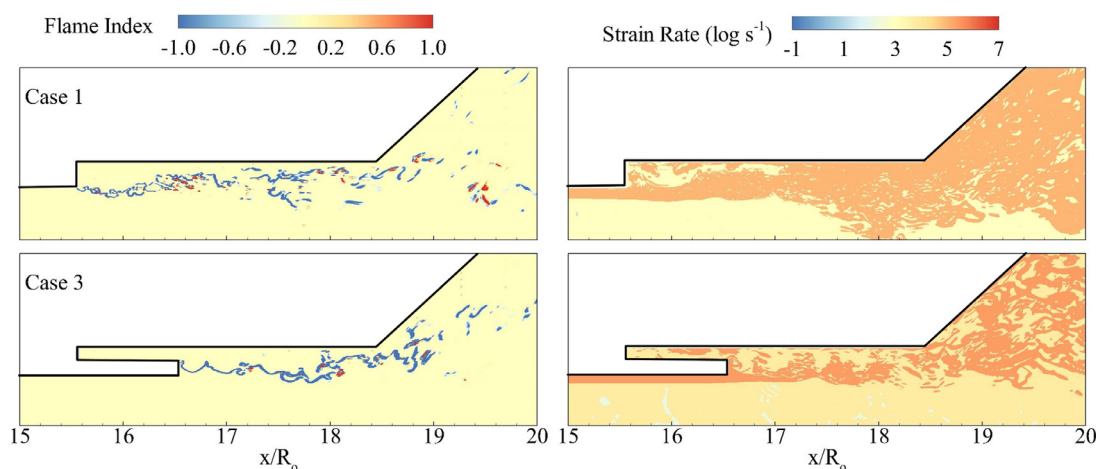


Fig. 5. Instantaneous distributions of flame index and magnitude of local strain rate (log space) for Cases 1 and 3.

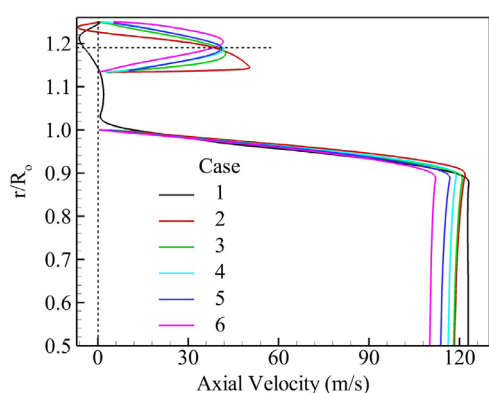


Fig. 6. Radial profiles of time-averaged axial velocity immediately downstream (Case 1) or upstream (Cases 2–6) of the GOX post tip.

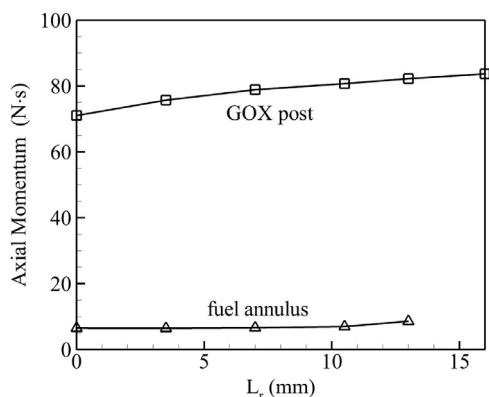


Fig. 7. Time-averaged bulk axial momentum immediately upstream of the end of GOX post as a function of recess length.

triggers momentum transfer from the angular to the axial component [29]. This gain overshadows the viscous loss along the annulus surface, and leads to the slight increase in axial momentum at the fuel annulus exit.

4.2. Recess region

Figure 8 shows snapshots of the temperature and mixture-fraction fields in the recess region for all cases. The arrow denotes the location of the kerosene injection slit. Because of relatively low strain rate and adiabatic thermal boundary condition, the flame is

always anchored near the GOX post tip, the axial location of which moves downstream with decreasing recess length. It then develops in the mixing layer between the GOX and kerosene. The flame structures are largely induced by the shear-layer instabilities, originating from various mechanisms of flow convection, baroclinicity, and volume dilation. The latter two were found to be substantial in vorticity production at supercritical conditions [35]. Kerosene is entrained into the GOX stream through various sizes of vortical motions, while GOX expands radially into the kerosene stream through mass diffusion and turbulent mixing. The kerosene stream forms a thin liquid film along the annulus outer surface due to the swirl-induced centrifugal force. The film is axially accelerated by the shear-layer growth as the film convects downstream. The film thickness decreases because of mass conservation, and the mixing region increases accordingly.

Figure 9 shows the distributions of time-mean mixture fraction and azimuthal velocity for all cases. The dashed lines denote the iso-surface of 0.8 enclosing the kerosene-rich mixture. The axial penetration of this mixture fraction decreases with increasing recess length. The maximum mixture fraction at the exit of the recess region is less than 0.8 when the shielding length is less than 3 mm. The kerosene is nearly depleted through decomposition and oxidation in the recess region for Cases 1 and 2 ($L_r \geq 13$ mm). The kerosene film thickness first increases and then decreases as it issues from the annulus for all cases with recess. In the area close to the post tip, the shear-layer induced by the azimuthal velocity difference across the mixing zone decelerates the kerosene film. The decrease in azimuthal velocity reduces the swirl strength and centrifugal force, leading to the thickening of the film. On the other hand, the kerosene oxidation and diffusion thins the film. The thickening effect first overshadows the thinning effects until the film thickness reaches a maximum value. The extensive burning and turbulent mixing then becomes prevalent and diminishes the kerosene film.

Figure 10 shows the radial distribution of mixture fraction at the exit of the recess region for all cases. The pink dashed line for Case 6 represents a discontinuity, where GOX in the center post has not yet interacted with kerosene in the annulus. The region with finite gradient of mixture fraction indicates the presence of a mixed state. Case 1 has the widest radial span of finite gradient among the six cases. This span decreases with decreasing recess length, and becomes zero for Case 6. The maximum mixture fraction on the outer surface of the annulus ($R_f/R_o = 1.25$) consistently decreases with increasing recess length. Therefore, the longer the recess, the higher the mixing efficiency. This observation is also supported by the increase of flame area with recess length, as seen

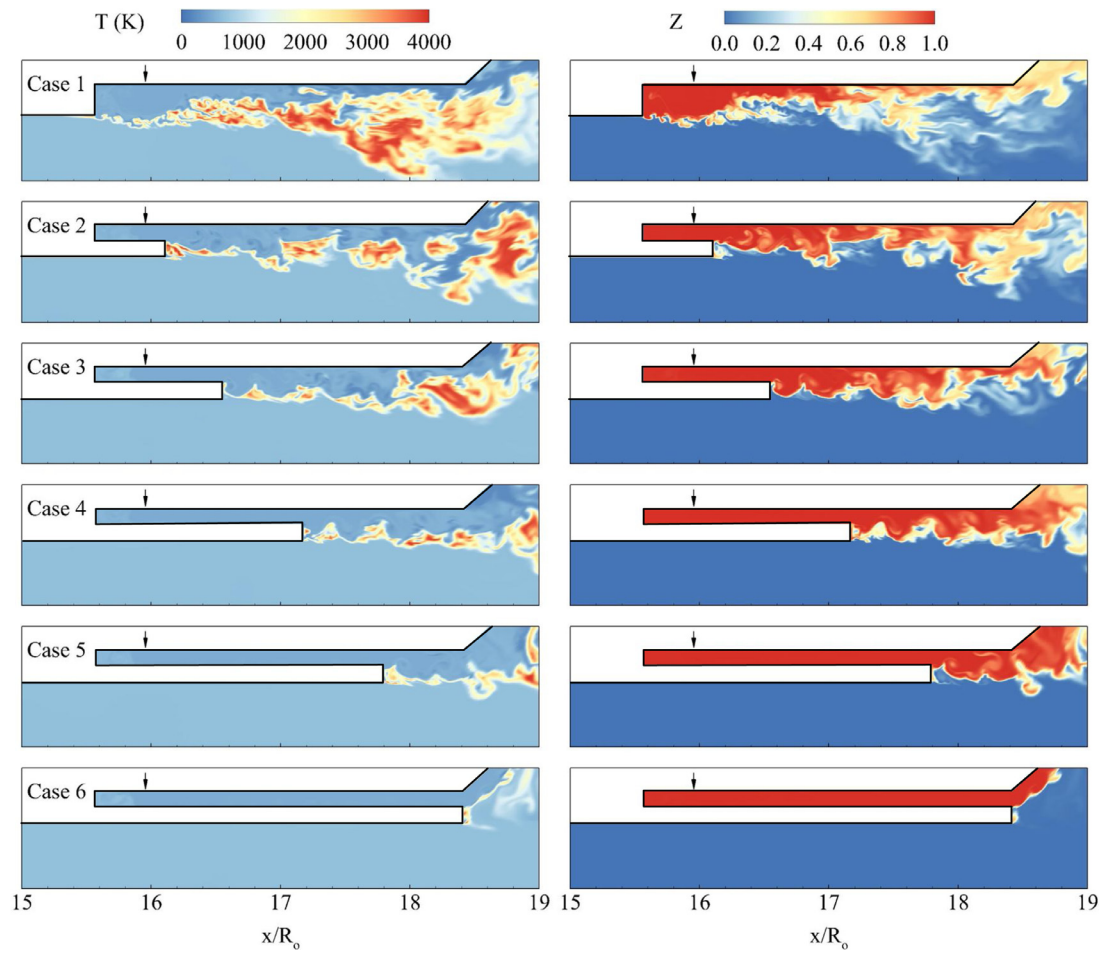


Fig. 8. Snapshots of temperature (left) and mixture fraction (right) fields in recess region for all cases.

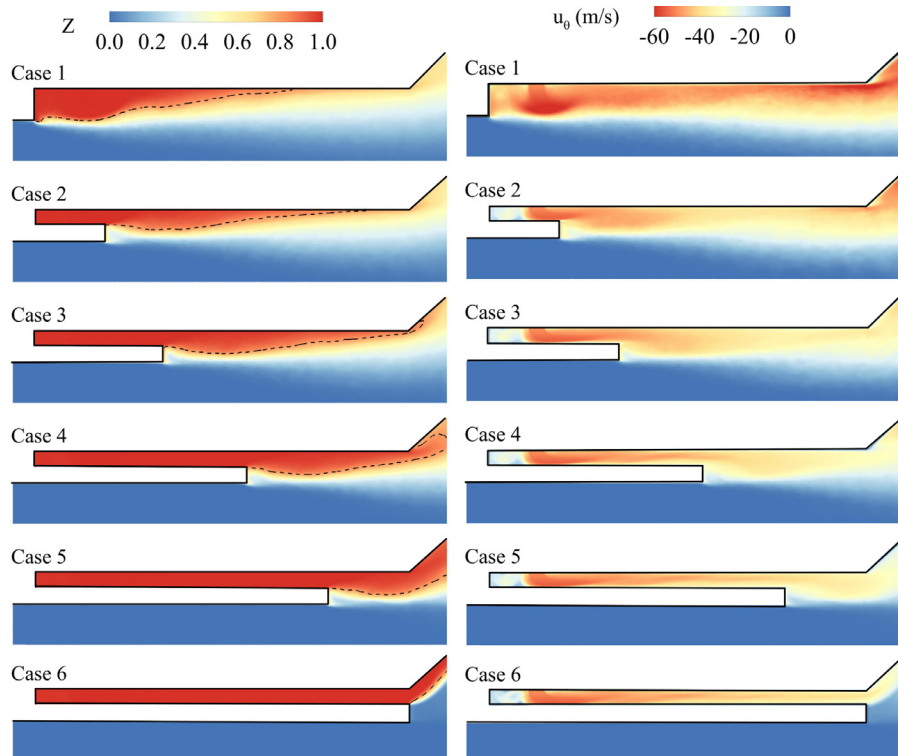


Fig. 9. Distributions of time-mean mixture fraction and azimuthal velocity in recess region for all cases (Dashed lines: iso-surface for mixture fraction of 0.8).

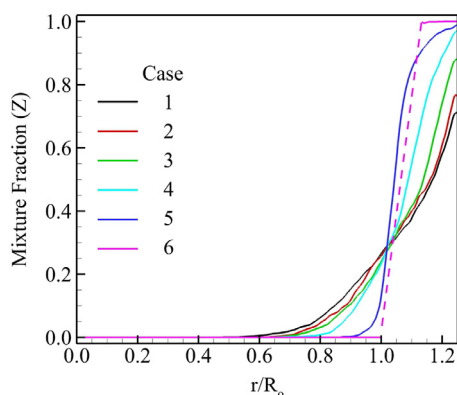


Fig. 10. Radial distributions of mixture fraction at exit of recess region for all cases.

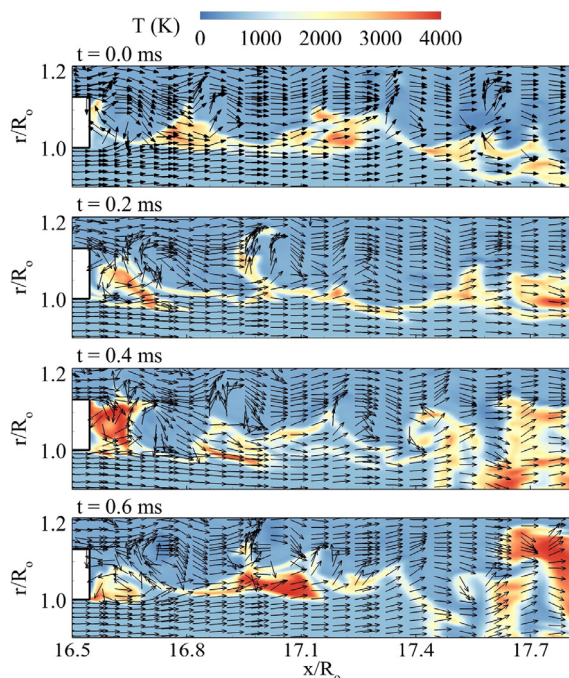


Fig. 11. Temporal evolution of temperature field overlaid by velocity vectors in recess region for Case 3.

in Fig. 8. Intensive combustion is initiated in the recess region, while it is delayed to the taper region for Case 6 (with no recess).

The flow evolution offers more insight into the flame initialization process. Figure 11 shows the temporal evolution of the temperature field overlapped by the velocity vectors for Case 3. Here $t=0$ ms is an arbitrary reference point after the flame is sufficiently developed. At $t=0$ ms, the flame is detached from the GOX post tip. Between them, a recirculation zone is formed, which in turn enhances the mixing between GOX and kerosene. At $t=0.2$ ms, the flame moves upstream, as a result of the enhanced mixing, but remains detached. It becomes fully attached to the post at 0.4 ms, at which point the mixing reaches the optimal state. After extensive consumption of the reactants, the flame shifts downstream and another flame cycle begins. Large vortical motions arising from the shear-layer instability in the mixing region play an important role in stabilizing the flame. These vortices provide a longer residence time for the interaction of GOX and kerosene. It is concluded that the flame is initiated and stabilized by the intensive vortical motions in the wake of the GOX post. This observation was corroborated qualitatively using optical diagnostics, in a recent study of the flame dynamics of a geometrically similar

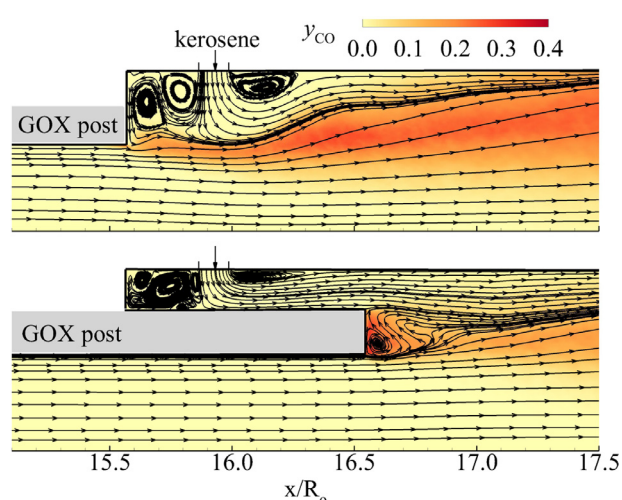


Fig. 12. Time-averaged CO mass fraction distribution superimposed by streamlines for Cases 1 (top) and 3 (bottom).

injector [10]. The wrinkled flame is transported downstream and induces a broader combustion zone in the taper region, where the propellants have sufficiently mixed.

Figure 12 shows the time-averaged distribution of the CO mass fraction, superimposed with streamlines in the recess region for Cases 1 and 3. For Case 1 with no fuel shielding ($L_r = 16$ mm), the end of the GOX post is radially aligned with the headend of the fuel annulus. The flow pattern is similar to that of a liquid jet in a crossflow. The kerosene penetration depth is roughly equivalent to the height of the rear-facing step. The injected kerosene is divided into two branches. One flows upstream to the headend and generates two large recirculating bubbles. The flow residence time in this zone is on the order of magnitude of the ignition time delay of reactants, allowing sufficient mixing between GOX and kerosene to activate ignition. The other branch, containing the majority of the kerosene stream, travels downstream along with the GOX stream. Case 3 presents a significantly different flow pattern due to the presence of fuel shielding. The swirling fuel flow moves downstream in the annulus. A small recirculating bubble is established next to the lower part of the GOX post tip. This low-speed zone provides sufficient time for reactant mixing and anchors the flame in a robust manner, as manifested by the high concentration of CO in Fig. 12. Similar flow patterns are observed for other cases with fuel shielding. The situation differs from that in a bi-swirl injector in which two-counter rotating bubbles occurs in the wake of the inner swirler [13].

4.3. Taper region

The flame is further developed in the taper region, which serves several purposes. First, the taper adjusts the fuel spreading angle to a desired value to facilitate injector inter-element mixing (42° in the present study). Note that the prescribed spreading angle of the fuel injected into the downstream region should exceed the taper angle, so that the fuel flows along the injector surface to provide thermal protection. Second, the taper region provides necessary damping of acoustic oscillations originating from the intensive combustion in the downstream chamber. The acoustic energy can be dissipated and/or convected by the vortex motions in the taper region.

Figure 13 shows the distributions of the time-averaged mixture fraction in the taper region for all cases. As previously discussed in connection with Fig. 9, the extent of combustion near the entrance of the taper region improves as the recess length increases.

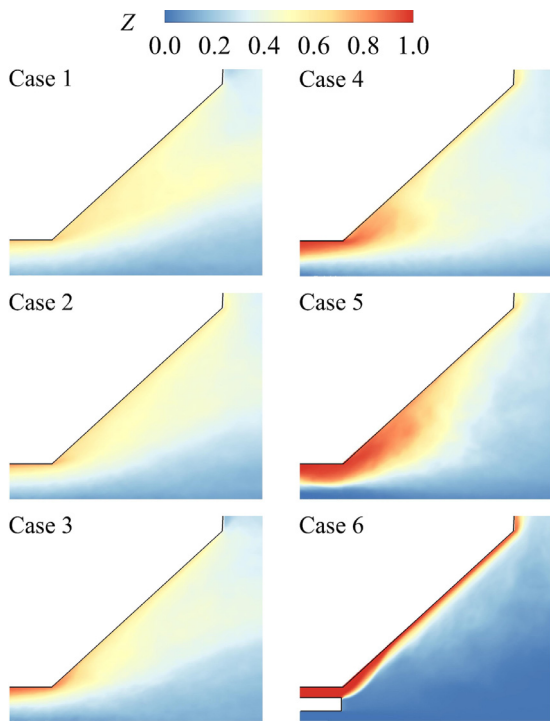


Fig. 13. Time-averaged mixture fraction distributions in taper region for all cases.

The mixture fraction along the taper surface decreases accordingly. In particular, for Case 6 (no recess, $L_r = 0$), the kerosene fuel travels along the taper surface and then along the injector faceplate in the downstream region, due to the swirl-induced centrifugal force. The kerosene and GOX barely mix. The GOX flows primarily in the axial direction, but the kerosene spreads outward. This situation is undesirable in practical applications, and underlines the necessity of a recess for the current injector prototype.

For Cases (1–5) with a recess region, a certain level of combustion is established upstream of the taper region. Although the mixture fraction along the taper surface decreases from Case 1 to Case 6, it is always larger than the stoichiometric mixture fraction. The temperature near the taper surface is thus relatively low. This is demonstrated by the snapshot of the temperature field in Fig. 14. The higher mixture fraction protects the taper surface from being overheated by the hot products in the flame region, reducing cooling requirements and prolonging the life of the device. Case 1 shows a more distributed burning area than does Case 3, and this is consistent with the earlier observation that Case 1 achieves better mixedness in the recess region.

Another important role of the taper is to stabilize the flame. Figure 15 shows instantaneous streamlines in the taper region for Cases 1 and 3. Various recirculation zones next to the taper surface are produced by flow separation, due to the decaying swirl strength and adverse pressure gradient in the streamwise direction. These zones contain burned products and act as a heat pool to preheat the cold propellant and sustain the combustion. The combined recess and taper regions provide the major flame stabilization mechanism. A small flame is initiated next to the GOX post tip in the recess region. When transported to the taper region, the flame is further developed and stabilized, leading to intensive combustion in the downstream region.

4.4. Downstream region

Figure 16 shows a snapshot of the temperature field in the downstream region for Cases 3 and 6. Intensive combustion oc-

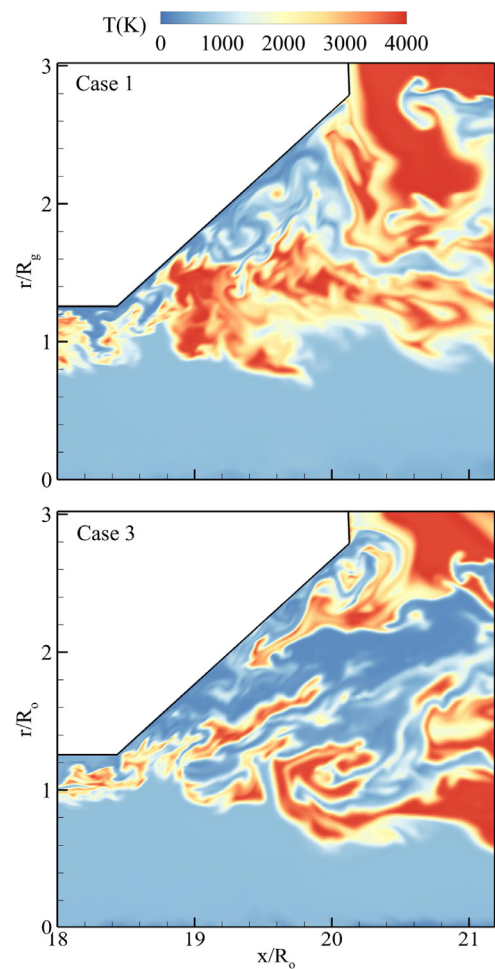


Fig. 14. Snapshots of temperature field in taper region for Cases 1 and 3.

cur over a broad area in both radial and axial directions in Case 3, while burning takes place only along a radial layer next to the injector faceplate in Case 6. In the latter case, kerosene primarily flows along the taper surface and then the faceplate, while GOX in the center post is transported downstream axially without much kerosene entrainment. The high-temperature region results from reactions between kerosene and oxygen in the downstream environment away from the center. A portion of combustion products are entrained into the central GOX stream through vortical motions originating from the wake of the post tip, as manifested by roll-up vortices with an intermediate temperature level near the center.

The flame characteristics can be further described by the stoichiometric mixing line since diffusion-dominated combustion prevails for all cases. Figure 17 shows the time-averaged stoichiometric lines extracted across the flame field. For Cases 1–4 with recess length larger than 3.5 mm, the flame is sustained in the further downstream region, while for Cases 5 and 6 the flame starts to bend up radially before $x/R_0 = 20$. For a larger recess length, kerosene is significantly swept in the shear layer and carried to the downstream region for complete combustion. For a smaller recess length (or no recess), kerosene spreads upwards and the combustion efficiency between kerosene and GOX severely reduces. The recess is thus crucial for achieving effective mixing of propellants in an early stage and subsequent intensive combustion in the desired downstream region.

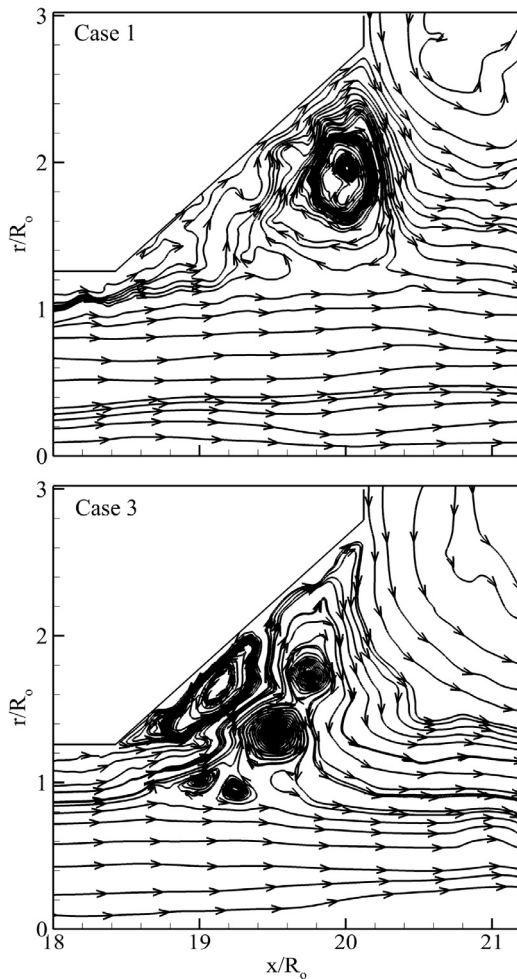


Fig. 15. Instantaneous streamlines in taper region for Cases 1 and 3.

5. Conclusion

The present work investigates the combustion characteristics of gas-centered liquid-swirl coaxial (GCLSC) injectors, with gaseous oxygen (GOX) and kerosene as propellants at supercritical pressure. This type of injectors has been broadly employed for current and future ORSC cycle engines. The analysis is based on a large-eddy-simulation technique for treating turbulent flows, and a steady laminar flamelet approach is employed for turbulence/chemistry interactions. Flow structures and flame dynamics are examined in detail. The flowfield can be divided into four regimes: propellant injection, flame initialization, flame development, and intensive combustion. The flame is stabilized near the post tip in the recess region and further enhanced in the taper region. Fuel-rich

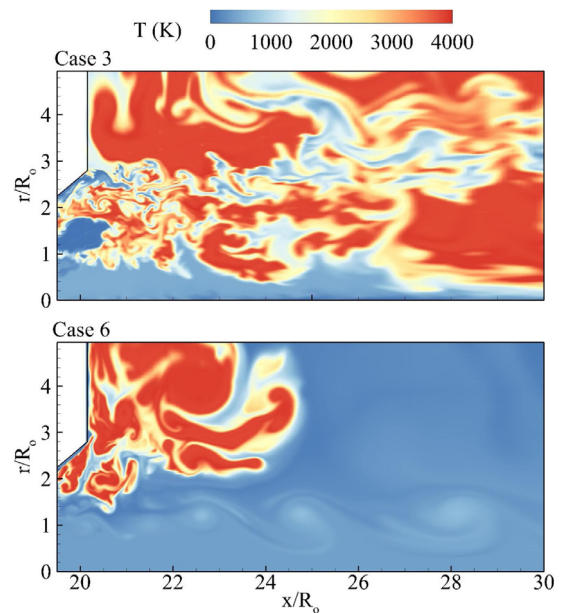


Fig. 16. Snapshot of temperature in downstream region for Cases 3 and 6.

mixtures travel along the surface of the injector due to the swirl-induced centrifugal force, and provide thermal protection to the surface from the flame zone.

The effects of recess (or fuel-shielding) length on the flow and flame dynamics are explored in depth. As the recess length increases, the efficiency of mixing and combustion improves significantly. The kerosene film is nearly depleted at the entrance of the taper region when recess length is longer than 13 mm, and the flame evolves upwards radially when the recess length is lower than 3.5 mm. The latter is caused by insufficient mixing between GOX and kerosene before they enter the taper region. In a fully recessed injector without fuel shielding, two recirculation zones containing kerosene-rich mixture are formed between the injection slit and the headend. The kerosene penetration depth is on the order of magnitude of the thickness of the GOX post. A broadly distributed flame is established at the exit of the recess region with a maximum mixture fraction less than 0.8. For a non-recessed injector with full fuel shielding, the occurrence of combustion is delayed to the taper region. The flame resides along the taper surface and the faceplate, leaving the majority of the GOX convecting downstream without burning. This situation is undesirable in practical designs, and underlines the necessity of an appropriate recess region in a high-performance injector.

Acknowledgments

This work was sponsored partly by the Air Force Office of Scientific Research under Grant No. FA 9550-10-1-0179, and partly by

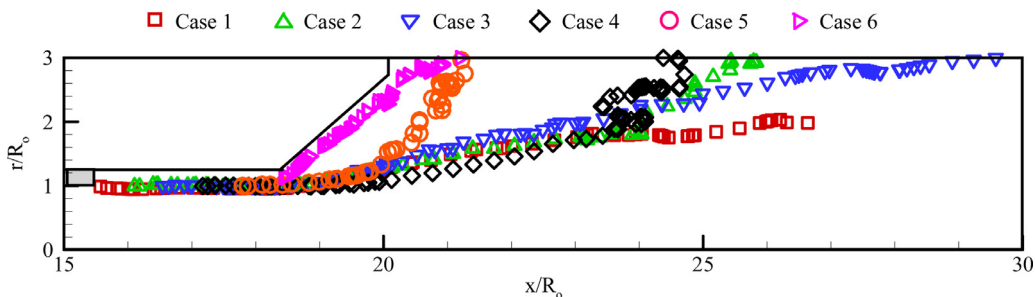


Fig. 17. Time-averaged stoichiometric lines for all cases.

the William R. T. Oakes Endowment of the Georgia Institute of Technology. The authors gratefully acknowledge support and advice from Mitat A. Birkan.

References

- [1] M.L. Dranovsky, V. Yang, F. Culick, D.G. Talley, Combustion instabilities in liquid rocket engines: testing and development practices in Russia, *Progr. Astronaut. Aeronaut.* 221 (2007) 253–281 AIAA.
- [2] V. Yang, W.E. Anderson, Liquid rocket engine combustion instability, *Progr. Astronaut. Aeronaut.* 169 (1995) AIAA.
- [3] V.G. Bazarov, V. Yang, Liquid-propellant rocket engine injector dynamics, *J. Propul. Power* 14 (1998) 797–806.
- [4] K. Miller, J. Sisco, N. Nugent, W. Anderson, Combustion instability with a single-element swirl injector, *J. Propul. Power* 23 (2007) 1102–1112.
- [5] J.C. Sisco, Y. Yu, V. Sankaran, W.E. Anderson, Examination of mode shapes in an unstable model combustor, *J. Sound Vib.* 330 (2011) 61–74.
- [6] Y. Yu, J.C. Sisco, S. Rosen, A. Madhav, W.E. Anderson, Spontaneous longitudinal combustion instability in a continuously-variable resonance combustor, *J. Propul. Power* 28 (2012) 876–887.
- [7] R. Garby, L. Selle, T. Poinso, Large-Eddy Simulation of combustion instabilities in a variable-length combustor, *Comptes Rendus Mécanique* 341 (2013) 220–229.
- [8] M.E. Harvazinski, C. Huang, V. Sankaran, T.W. Feldman, W.E. Anderson, C.L. Merkle, D.G. Talley, Coupling between hydrodynamics, acoustics, and heat release in a self-excited unstable combustor, *Phys. Fluids* 27 (2015) 045102.
- [9] D. Manski, C. Goertz, H.-D. Sabnick, J.R. Hulka, B.D. Goracke, D.J.H. Leveck, Cycles for earth-to-orbit propulsion, *J. Propul. Power* 14 (1998) 588–604.
- [10] H.C. Ballance, O. Bibik, T.S. Cook, S. Danczyk, S.A. Schumaker, V. Yang, T.C. Lieuwen, High speed optical diagnostics of high pressure gaseous-oxygen (GOX) center, liquid-kerosene swirl injector, *J. Propul. Power* (2018) submitted for publication.
- [11] K. Ahn, S. Seo, H.-S. Choi, Fuel-rich combustion characteristics of biswirl coaxial injectors, *J. Propul. Power* 27 (2011) 864–872.
- [12] K. Ahn, J.-G. Kim, H.-S. Choi, Effects of injector recess on heat flux in a combustion chamber with cooling channels, *Aerosp. Sci. Technol.* 37 (2014) 110–116.
- [13] X. Wang, V. Yang, Supercritical mixing and combustion of liquid-oxygen/kerosene bi-swirl injectors, *J. Propul. Power* 33 (2016) 316–322.
- [14] X. Wang, Y. Li, Y. Wang, V. Yang, Near-field flame dynamics of liquid oxygen/kerosene bi-swirl injectors at supercritical conditions, *Combust. Flame* 190 (2018) 1–11.
- [15] S. Soller, R. Wagner, H.-P. Kau, P. Martin, C. Maeding, Combustion stability characteristics of coax-swirl-injectors for oxygen/kerosene, *AIAA Paper* (2007) 5563.
- [16] L. Zhang, X. Wang, Y. Li, S.-T. Yeh, V. Yang, Supercritical fluid flow dynamics and mixing in gas-centered liquid-swirl coaxial injectors, *Phys. Fluids* 30 (7) (2018) 075106.
- [17] Y. Li, X. Wang, L. Zhang, S.-T. Yeh, V. Yang, A parametric study of gas-centered liquid-swirl coaxial injector flow dynamics at supercritical conditions, *AIAA J.* (2017) submitted for publication.
- [18] J.C. Oefelein, V. Yang, Modeling high-pressure mixing and combustion processes in liquid rocket engines, *J. Propul. Power* 14 (1998) 843–857.
- [19] V. Yang, Modeling of supercritical vaporization, mixing, and combustion processes in liquid-fueled propulsion systems, *Proc. Combust. Inst.* 28 (2000) 925–942.
- [20] T. Poinso, D. Veynante, *Theoretical and numerical combustion*, RT Edwards, Inc, 2005.
- [21] X. Wang, H. Huo, V. Yang, Counterflow diffusion flames of oxygen and n-alkane hydrocarbons (CH₄-C₁₆H₃₄) at subcritical and supercritical conditions, *Combust. Sci. Technol.* 187 (2014) 60–82.
- [22] H. Huo, V. Yang, Large-eddy simulation of supercritical combustion: Model validation against gaseous H₂-O₂ injector, *J. Propul. Power* 33 (2017) 1272–1284.
- [23] P. Dagaut, A. El Bakali, A. Ristori, The combustion of kerosene: Experimental results and kinetic modelling using 1-to 3-component surrogate model fuels, *Fuel* 85 (2006) 944–956.
- [24] Q.-D. Wang, Y.-M. Fang, F. Wang, X.-Y. Li, Skeletal mechanism generation for high-temperature oxidation of kerosene surrogates, *Combust. Flame* 159 (2012) 91–102.
- [25] H. Huo, X. Wang, V. Yang, A general study of counterflow diffusion flames at subcritical and supercritical conditions: oxygen/hydrogen mixtures, *Combust. Flame* 161 (2014) 3040–3050.
- [26] H. Meng, V. Yang, A unified treatment of general fluid thermodynamics and its application to a preconditioning scheme, *J. Comput. Phys.* 189 (2003) 277–304.
- [27] S.-Y. Hsieh, V. Yang, A preconditioned flux-differencing scheme for chemically reacting flows at all mach numbers, *Int. J. Comput. Fluid Dyn.* 8 (1997) 31–49.
- [28] N. Zong, V. Yang, An efficient preconditioning scheme for real-fluid mixtures using primitive pressure-temperature variables, *Int. J. Comput. Fluid Dyn.* 21 (2007) 217–230.
- [29] N. Zong, V. Yang, Cryogenic fluid dynamics of pressure swirl injectors at supercritical conditions, *Phys. Fluids* 20 (2008) 056103.
- [30] A.M. Ruiz, G. Lacaze, J.C. Oefelein, R.I. Mari, B. Cuenot, L. Selle, T. Poinso, Numerical benchmark for high-Reynolds-number supercritical flows with large density gradients, *AIAA J.* 54 (5) (2015) 1445–1460.
- [31] H.-G. Li, P. Khare, H.-G. Sung, V. Yang, A large-eddy-simulation study of combustion dynamics of bluff-body stabilized flames, *Combust. Sci. Technol.* 188 (2016) 924–952.
- [32] H.G. Li, N. Zong, X.Y. Lu, V. Yang, A consistent characteristic boundary condition for general fluid mixture and its implementation in a preconditioning scheme, *Adv. Appl. Math. Mech.* 4 (2012) 72–92.
- [33] D.J. Bodony, Analysis of sponge zones for computational fluid mechanics, *J. Comput. Phys.* 212 (2006) 681–702.
- [34] H. Yamashita, M. Shimada, T. Takeno, A numerical study on flame stability at the transition point of jet diffusion flames, *Symp. (Int.) Combust.* 26 (1996) 27–34.
- [35] X. Wang, H. Huo, Y. Wang, V. Yang, Comprehensive study of cryogenic fluid dynamics of swirl injectors at supercritical conditions, *AIAA J.* 55 (2017) 3109–3119.